Technical Physics, 2022, Vol. 67, No. 4

01

The thermal image receiver realized in the Image intensifier tube architecture

© *A.S. Grevcev, P.A. Zolotukhin, E.A. Il'ichev, G.N. Petrukhin, A.V. Popov, G.S. Rychkov*

National Research University of Electronic Technology — MIET
Zelenograd, Moscow, Russia
e-mail: edil44@mail.ru, alexcoretex@gmail.com

Received October 22, 2021
Revised November 5, 2021
Accepted January 10, 2022

An innovative design of thermal imaging is considered. The results of analysis and calculations of the characteristics of a thermal image receiver ($3-15\,\mu$m), made in the electron-optical converter architecture, are presented. The spatial dependences of the spontaneous polarization the electric field strengths and the electric potentials on the surface of pyroelectric film are calculated. The characteristics of thermal-field-induced polarization of various pyroelectric films are obtained. The temperature dependences of various pyroelectric films polarizations are calculated by the COMSOL Multiphysics software package based on the finite element method. The possible influences of the piezoelectric effect to the images of the distribution of electric potentials of pyroelectric films are taken into account. The estimates of the values of the main characteristics of the image intensifier tube architecture are obtained.

Keywords: the image intensifier tube, spontaneous polarization, pyroelectric, bolometric thermal imagers, pyroelectric thermal imagers.

DOI: 10.21883/TP.2022.04.53597.270-21

Introduction

The development of a competitive and uncooled thermal image receiver sensible within the spectral range of $3-15\,\mu$m is a relevant objective. The currently available designs of thermal image receivers may be classified into three groups: photonic receivers based on narrow-bandgap semiconductors, quantum wells in multilayer heterostructures, doped semiconductors, or Schottky diodes; bolometric resistive receivers based on superconducting and semiconducting materials; and pyroelectric receivers based on the polarization effect of a sensor-converter film. All thermal receivers, except the sensors based on pyroelectric films, require deep cooling down to helium temperatures [1-13].

1. State-of-the-art in thermal imaging systems

The performance limits of the currently available thermal image receivers of the mentioned classes are presented in Tables 1 and 2. Specifically, Table 1 lists the characteristics of thermal image receivers based on generation–recombination processes, where the signal being measured as the nonequilibrium carrier current.

The characteristics of thermal image receivers with sensors operating based on thermoresistive and polarization effects are listed in Table 2. Uncooled thermal image receivers based on ferro- and pyroelectric materials are also presented here.

The data in Tables 1 and 2 demonstrate that the key performance limits for thermal image receivers differ significantly. This is due to the difference in the physical effects underlying the processes of detecting and converting thermal images through their sensing elements. For example, the pyroelectric vidicons with capacitive reading require a deep modulation of the input signal intensity that increases the mass and size and energy consumption of these devices. In the case of photonic and resistive receivers, their operation requires deep cooling (down to $1-4$ K).

All available thermal imaging systems have a common disadvantage — that all of them require an additional channel for observing the surrounding terrain.

2. Design, physical model of processes, and calculation results

2.1. Design, operating principle

An alternative design of a thermal image receiver in the image intensifier tube (IIT) architecture is proposed and discussed below. Its schematic diagram is shown in Fig. 1. Images of a „radiating" thermal object and its local environment (in reflected night sky light), are focused by the optical-mechanical system of the thermal receiver, on a pyroelectric film and a photocathode, respectively. Thus, this compact and innovative uncooled thermal receiver offers the possibility to detect images of a thermal object in a single-channel design with the images of its surrounding terrain.

Table 1. Key characteristics of different designs of photonic receivers in the thermal range

Thermal imager type	$\mathscr{R}^*$, A/W	D^{**}, cm $\cdot$ Hz$^{1/2}$, W	Operating spectral range, μm	Operating temperature, K	NETD***, mK	NEP****, fW/Hz$^{1/2}$
QWIP InP/InGaAs	8 [1], 2.9 [2]	$7 \cdot 10^{10}$ [1]	8 [1]	80 [1]	28 [3]	–
Blocked impurity band (BIB) Ge:Ga	17 [3]	$4 \cdot 10^{10}$ [4]	14–140 [4]	1.5 [3]	–	0.05 [5]
BIB Si:Sb	6 [6]	$2.9 \cdot 10^{10}$ [4]	15–40 [4]	5 [7]	–	0.056 [5]
BIB Si:As	5 [8]	$2.8 \cdot 10^{10}$ [4], 10^{14} [9]	2–25 [10]	7–10 [9]	–	0.04 [5]
Thermal imagers based on InSb photodiodes	$\sim$ 1–2 [11]	10^{11}	1–5 [10]	0.6–77 [10]	14.6 [12]	800 [13]

Note. *$\mathscr{R}$ — sensitivity of a thermal imager, **D — detectivity, ***NETD — noise-equivalent temperature difference (temperature sensitivity threshold), ****NEP — noise-equivalent power.

Table 2. Key characteristics of different designs of thermal image receivers operating based on thermoresistive capacitive, and polarization effects

Thermal imager type	$\mathscr{R}$, V/W	D, cm $\cdot$ Hz$^{1/2}$/W	Operating temperatures, K	NETD, mK	NEP, pW/Hz$^{1/2}$
Bolometric thermal imagers (capacitive, VO_x)	> 1000 [14]	$9.11 \cdot 10^8$ [15]	Room temperature [15]	99 [16]	50 [15]
Bolometric thermal imagers (capacitive, Si*)	10^6 [18]	$2.4 \cdot 10^9$ [18]	Room temperature [17]	50 [17]	2 [18]
Bolometric thermal imagers (resistive, based on GaAs)	$\sim$ 1800 [19]	10^9–$2 \cdot 10^{10}$ [19]	150 [19]	–	50 [20]
Bolometric thermal imagers (resistive, based on Ge*)	4500 [21]	$8 \cdot 10^{11}$ [21]	2 [21]	–	0.5 [21]
Bolometric thermal imagers (Si/Au barrier)	$8 \cdot 10^8$ [22]	–	4 [22]	0.13 [22]	$60 \cdot 10^{-6}$ [22]
Pyroelectric detectors, $LiTaO_3$ (capacitive readout)	1000	$6 \cdot 10^9$ [23]	Room temperature	37 [24]	13 000 [25]
Pyroelectric thermal imagers, $LiNbO_3$ (capacitive readout)	7020 [26]	$7.76 \cdot 10^7$ [26]	Room temperature	–	2000 [26]
Pyroelectric thermal imagers, PZT (capacitive readout)	1000–100 [27]	$\sim 2 \cdot 10^9$ [27]	Room temperature	–	25 [27]
Pyroelectric thermal imagers, TGS: *l*-alanine (capacitive readout)	50–300	$\sim 10^9$ [23]	Room temperature	–	540

Note. The notation is the same as in Table 1.

The thermal object image pattern induces polarization of pyroelectric film and generates a surface electric potential relief identical to the distribution of the thermal image intensity over the sensor film surface. The optical image of the environment focused on the photocathode plane, which converted the optical image into photoelectrons flux. The flux of photoelectrons is directed to the surface of the pyroelectric film and used as a readout instrument of the distribution pattern of electric potentials that is identical to the distribution pattern of radiating power of the thermal object.

Following the interaction with the potential relief the flux of photoelectrons is read out by the electric field through apertures in the pyroelectric film and its silicon membrane in the direction of a microchannel Plate (MCP). The flux of photoelectrons, which contains information on both the thermal object and its environment, is multiplied in the MCP. Then, it is directed to a cathodoluminescent screen, and converted photoelectrons flux into an optical image of the visible range. The obtained image may be digitized by using a CCD unit which is connected through a fiber-optic faceplate of the IIT output window.

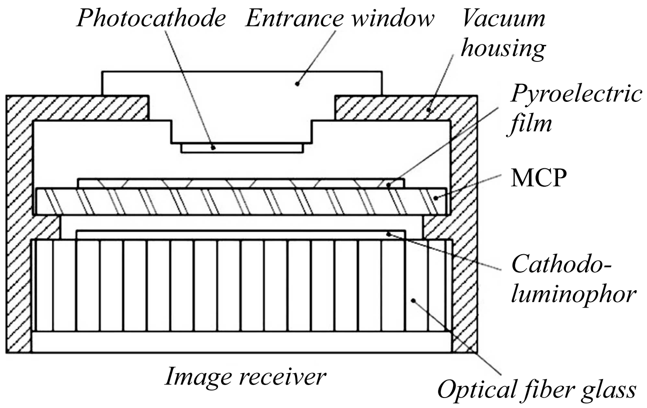

Figure 1. Design of the thermal image receiver in the IIT architecture.

2.2. Selection of key materials and its substantiation

Temperature polarization coefficients $d\varphi/dT$ and low values of the thermal conductivity coefficient should be the criteria for selection of pyroelectric films of uncooled thermal image receivers. Pyroelectric materials feature high values of spontaneous polarization P_S and a considerable pyroelectric coefficient $(p = dP_S/dT)$ and do not require cooling [28]. However, high values of spontaneous polarization P_S in standard systems (e.g., currently available vidicons) may affect the sensitivity threshold when the surface potential is read out with an electron flux.

Since polarization of matter is the result of a superposition of projections of matter dipoles onto a designated direction, the following expression for the magnitude of spontaneous polarization is true:

$$P_S = \frac{\sum\limits_{i=1}^{n} p_i}{V} = \frac{\sum\limits_{i=1}^{n} q_i d_i}{N(a+d)\Delta S} = \frac{qdn}{N(a+d)\Delta S} = \frac{qn}{\Delta S N}\,\frac{d}{(a+d)} = \frac{\sigma_S d}{a+d} = \sigma_S, \tag{1}$$

where n is the total number of dipoles, N is the number of dipole layers, d is the dipole displacement vector, a is the distance between dipole layers, ΔS is the film area, and σ_s is the surface charge density.

Thus, the coefficient of spontaneous polarization of a pyroelectric film (P_S) corresponds to the surface charge densities (σ_- and σ_+) on the outer surfaces of the dipole layer (even in the case of „thick" films). This allows one to retrieve information of the surface charge (and, consequently, the polarization coefficient) from tabulated P_S data for each specific pyroelectric material.

2.3. Functional dependences of the electric field potentials and intensity on the type of a pyroelectric film

Taking into account (1), we have developed a model of a dipole layer, which will consist of two oppositely charged planes of radius R, spaced from each other at a distance d, equal to the dipole displacement vector. This model was used to obtain the analytics expressions of the electric field and the electric potential on the surface of a pyroelectric film. As was demonstrated above, data on the surface charge density in a film may be retrieved from reference tables of spontaneous polarization values P_S.

On Fig 2 shows the model mentioned above, which makes it possible to obtain a functional dependence of the electric-field intensity at arbitrary distance Z from fragment dS of the upper charged plane of the dipole layer Fig. 2:

$$dE_{\text{upper plane}} = \frac{dq}{4\pi\varepsilon_0}\,\frac{1}{r_-^2}\cos(\theta), \tag{2}$$

where $\mathbf{r}_-$ is the radius vector from point z to designated unit area dS with coordinates (φ, r) on the upper plane with charge dq, ε_0 is the dielectric constant, and $\cos(\theta)$ is the cosine of the angle between vectors $\mathbf{r}_-$ and $\mathbf{r}$.

The relation between charge dq localized within area dS of the upper plane of the dipole layer and the spontaneous polarization coefficient in cylindrical coordinates is

$$dq = -\sigma dS = -P_S dS = -P_S J(\varphi, z) d\varphi dr = -P_S r d\varphi dr,$$

where dS is the element of area of the upper plate and $J(\varphi, \mathbf{r})$ is the Jacobian in cylindrical coordinates. Therefore, rewriting (2) in the form

$$dE_{\text{upper plane}} = -\frac{P_S r d\varphi dr}{4\pi\varepsilon_0}\,\frac{1}{r_-^2}\cos(\theta) = -\frac{P_S r d\varphi dr}{4\pi\varepsilon_0} \times \frac{1}{z^2+r^2}\,\frac{z}{\sqrt{z^2+r^2}},$$

we obtain the following relation (see Appendix 1) for the coordinate dependence of the electric-field intensity of the

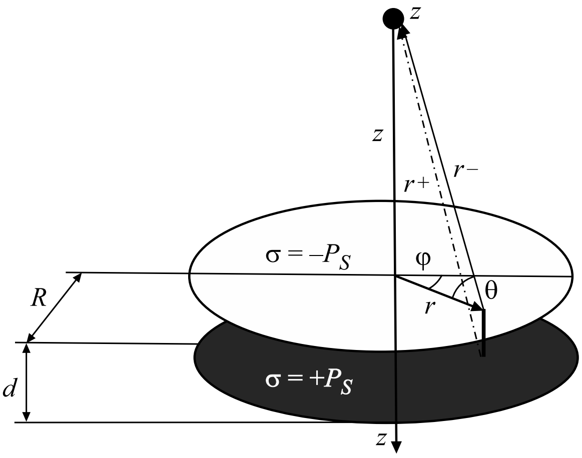

Figure 2. Dipole layer model for calculation of the surface potential at arbitrary point z.

upper plane of the dipole layer with radius R:

$$E_{\text{upper plane}} = \left(\frac{P_S}{2\varepsilon_0}\frac{z}{\sqrt{z^2+r^2}}\right)\Bigg|_0^R = -\frac{P_S}{2\varepsilon_0}\left(1-\frac{z}{\sqrt{z^2+R^2}}\right). \tag{3}$$

The coordinate dependence of the electric-field intensity of the lower (positively charged) plane of the dipole layer is obtained in a similar fashion:

$$E_{\text{lower plane}} = \frac{P_S}{2\varepsilon_0}\left(1-\frac{z+d}{\sqrt{(z+d)^2+R^2}}\right). \tag{4}$$

The superposition of fields (3) and (4) provides the coordinate dependence of total field $E_{\text{dip layer}}$ of the dipole layer:

$$E_{\text{dip layer}} = E_{\text{upper plane}} + E_{\text{lower plane}} = \frac{P_S}{2\varepsilon_0}\left(\frac{z}{\sqrt{z^2+R^2}} - \frac{z+d}{\sqrt{(z+d)^2+R^2}}\right). \tag{5}$$

If electric-field intensity (5) of the dipole layer, $E_{\text{dip layer}}$, is known, one may derive an expression for the electric potential at arbitrary coordinate point z. Using expression (5), we find the coordinate dependence of the electric potential on distance z to the dipole layer (see Appendix 2):

$$\varphi(z) = \frac{P_S}{2\varepsilon_0}\left(\sqrt{(z+d)^2+R^2} - \sqrt{z^2+R^2} - d\right). \tag{6}$$

Note that $\varphi(z) = 0$, which is a reasonable boundary condition, follows from (6) at $z \to \infty$.

Also it is important for applied problems to obtain approximations of the above analytical expressions of electric-field intensities and potentials on the dipole layer. The results of approximation were performed under the assumption that $R \gg z$ and $z \gg R$ and are presented below.

$R \gg z$ case

Presenting expression (5) in the form

$$E = \frac{P_S}{2\varepsilon_0}\frac{1}{\sqrt{z^2+R^2}}\left(z - \frac{z+d}{\sqrt{1+\frac{2zd+d^2}{z^2+R^2}}}\right)$$

following a series of transformations, we obtain (see Appendix 3):

$$E = \frac{P_S}{2\varepsilon_0}\frac{1}{R}\left(z - \frac{2(z+d)R^2}{2R^2+2zd+d^2}\right)$$

$$= -\frac{P_S}{2\varepsilon_0}\frac{2(z+d)R}{2R^2+2zd+d^2} = -\frac{P_S}{2\varepsilon_0}\frac{(z+d)}{R}.$$

Hence,
at $R \gg d \gg z$

$$E = -\frac{P_S}{2\varepsilon_0}\frac{d}{R}, \tag{7}$$

at $R \gg z \gg d$

$$E = -\frac{P_S}{2\varepsilon_0}\frac{z}{R}. \tag{8}$$

Proceeding in a similar way, we derive an approximation for the electric potential (see Appendix 3) from Eq. (6) at $R \gg z$:

$$\varphi(z) = \frac{P_S}{2\varepsilon_0}R\left(\frac{2zd+d^2}{2R^2} - \frac{d}{R}\right). \tag{9}$$

In the $2zd \gg d^2$ case, expression (9) takes the form

$$\varphi(z_0) = \frac{P_S}{2\varepsilon_0}\left(\frac{zd}{R} - d\right). \tag{10}$$

$z \gg R$ case

Let us rewrite expression (4) in the form

$$E_{\text{upper plane}} = -\frac{P_S}{2\varepsilon_0}\left(1 - \frac{z}{z\sqrt{1+\frac{R^2}{z^2}}}\right). \tag{11}$$

Expanding (11) into a Taylor series, we find

$$E_{\text{upper plane}} = -\frac{P_S}{2\varepsilon_0}\left(1 - \frac{z}{z\left(1+\frac{R^2}{2z^2}\right)}\right) = -\frac{P_S}{2\varepsilon_0}\left(\frac{R^2}{2z^2+R^2}\right).$$

and obtain the following at $z \gg R$:

$$E_{\text{upper plane}} = -\frac{P_S}{4\varepsilon_0}\frac{R^2}{z^2}. \tag{12}$$

Proceeding in a similar way within the indicated approximation ($z \gg R$), we determine the electric-field intensity produced by charged lower plane, $E_{\text{lower plane}}$, and the functional dependence of the total field of the dipole layer:

$$E_{\text{upper plane}} + E_{\text{lower plane}} = \frac{P_S R^2}{4\varepsilon_0}\left(\frac{1}{(z+d)^2} - \frac{1}{z^2}\right)$$

$$= \frac{P_S R^2}{4\varepsilon_0}\left(\frac{-2zd-d^2}{z^2(z+d)^2}\right),$$

which yields the following within the chosen approximations:

$$E = -\frac{P_S R^2}{2\varepsilon_0}\frac{d}{z^3}. \tag{13}$$

In order to derive the coordinate dependence of the electric potential in case $z \gg R$, we integrate expression (13) and find (see Appendix 4)

$$\varphi(z) = -\frac{P_S R^2}{4\varepsilon_0}\frac{d}{z^2}. \tag{14}$$

The final results of approximation of potentials and fields are presented in Table 3.

Table 3. Summary table of approximations of potentials and intensities of the electric field of the dipole layer

$z \gg R$		$R \gg z$ and $d \gg z$	
$\varphi(z)$ (14)	$E(z)$ (13)	$\varphi(z)$ (10)	$E(z)$ (7) (8)
$-\frac{P_S R^2}{4\varepsilon_0}\frac{d}{z^2}$	$-\frac{P_S R^2}{2\varepsilon_0}\frac{d}{z^3}$	$\frac{P_S d}{2\varepsilon_0}\left(\frac{z}{R}-1\right)$	$-\frac{P_S}{2\varepsilon_0}\frac{d}{R}$ or $-\frac{P_S}{2\varepsilon_0}\frac{z}{R}$

2.4. Calculations and graphical representation of the coordinate dependences of the electric field intensity and potentials

The functional dependences obtained above were used to calculate numerically the distributions of intensities of electric fields and electric potentials in the surroundings of sensing films. The parameters of pyroelectric films required for calculations are listed in Table 4.

When choosing the geometric size of a pyroelectric film and its silicon mesh semiconductor membrane, we took into account the shape and the size of the vacuum-tight housing of the image intensifier tube: the thickness of the mesh semiconductor membrane was $\sim 30\,\mu$m, the pyroelectric film thickness was $\sim 0.1-1.0\,\mu$m, and the radius of the film and the (Si/SiO_2) membrane was $R \approx 12.5$ mm.

Table 4. Key parameters of pyroelectric films

Material	Pyroelectric coefficient $p = dP_S/dT$, $\frac{\mu C}{m^2 K}$	Magnitude of spontaneous polarization-vector P_S, $\frac{C}{m^2}$
PZT-5H (Lead zirconate titanate)	−450 [29]	0.35 [29]
TGS with *l*-alanine (Triglycine sulfate)	−400 [29]	0.03 [29]
BSN50 (Barium strontium niobate)	−550 [29]	0.065 [28]

The calculated spatial distributions of electric potentials and electric-field intensities are presented below in Figs. 3–8. Their approximations (dashed lines) are shown in the same figures.

3. Analysis of the behavior of polarization processes induced by a thermal field in pyroelectric films

Let us estimate the changes in polarization and electric potentials of pyroelectric films — that are induced by a thermal field. We assume that the initial structure is a silicon membrane (with a radius of 12.5 mm and a thickness of 30 μm) with a silica layer ($\sim 1\,\mu$m in thickness) and a pyroelectric film ($\sim 1\,\mu$m in thickness) positioned in this order on top of it.

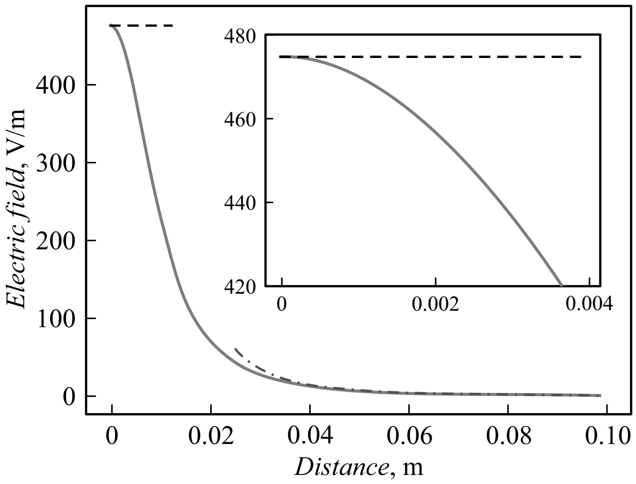

Figure 3. Distance dependence of the electric-field intensity of the dipole layer at arbitrary point z for PZT-5H.

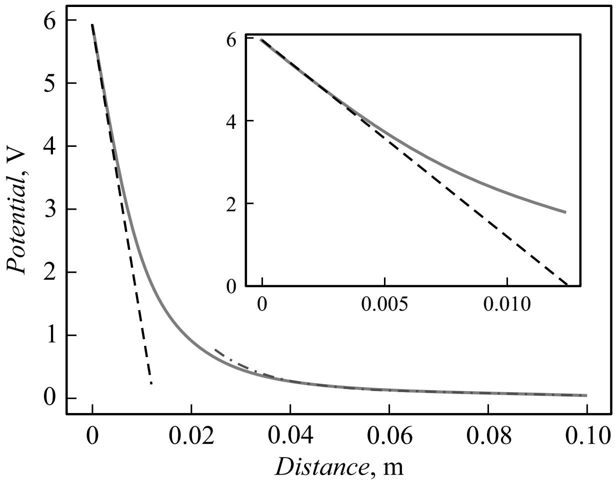

Figure 4. Distance dependence of the electric potential of the dipole layer at arbitrary point z for PZT-5H.

Let us use the heat balance equation to determine the dynamics of heating of the device structure:

$$\rho C_\rho \frac{dT}{dt} + \nabla(\mathbf{q} + \mathbf{q}_r) = \gamma P. \tag{15}$$

Here, $\mathbf{q}$ denotes the heat flux losses due to thermal conductivity of the structure

$$\mathbf{q} = -G\nabla T, \tag{16}$$

G is the thermal conductivity coefficient of the multilayer structure, ρ is density, C_ρ is thermal conductivity, $\mathbf{q}_r$ denotes the heat flux losses associated with radiation (estimated in the Stefan–Boltzmann approximation)

$$\mathbf{q}_r\mathbf{n} = \gamma\sigma(T^4 - T^4_{\text{initial}}), \tag{17}$$

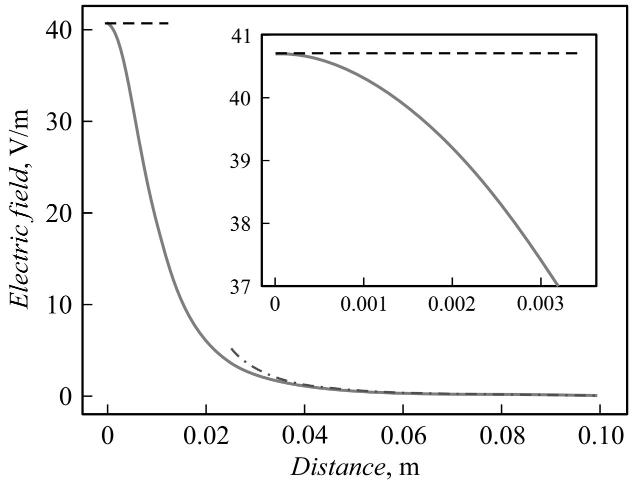

Figure 5. Distance dependence of the electric-field intensity of the dipole layer at arbitrary point z for TGS with l-alanine.

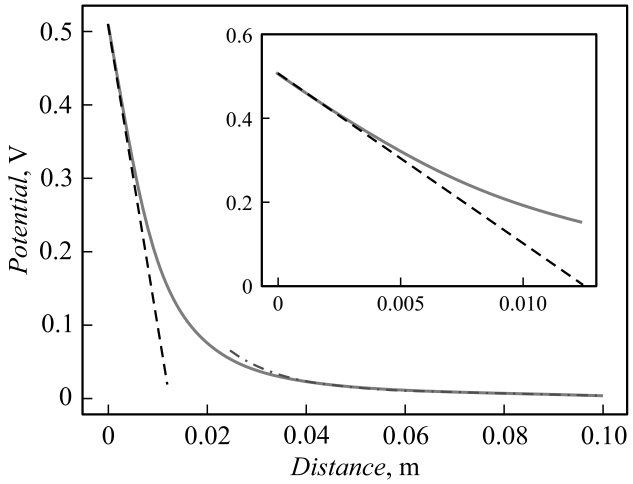

Figure 6. Distance dependence of the electric potential of the dipole layer at arbitrary point z for TGS with l-alanine.

n is the unit normal vector to the surface of the studied structure, T_{initial} is the initial temperature, T is the current temperature of the sensing and conversion layer, σ is the Stefan–Boltzmann constant, and γ is the emissivity of the sensor film surface.

The thermal resistance model (see its graphical representation in Fig. 9) with heat flux (16) is presented as the density of current passing through a number of thermal resistances connected in series. Thus, the heat flux may formally be presented as a ratio of the difference in temperature between the upper and the lower film layers to the sum of thermal resistances of the multilayer structure.

The parameters characterizing the considered pyroelectric materials are listed in Table 5, the heat flux incident on the sensing and conversion film was assumed to be equal to $0.21\,\mu\text{W/cm}^2$ (the total incident heat flow rate is

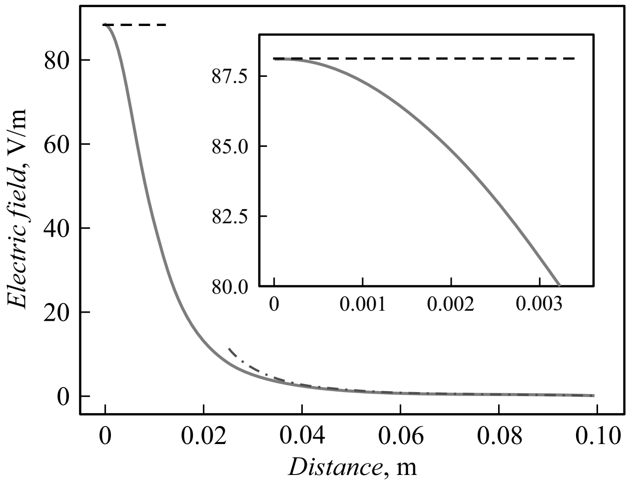

Figure 7. Distance dependence of the electric-field intensity of the dipole layer at arbitrary point z for BSN50.

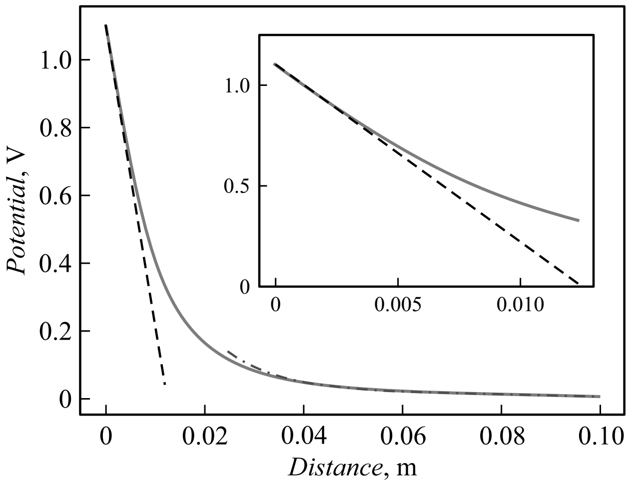

Figure 8. Distance dependence of the electric potential of the dipole layer at arbitrary point z for BSN50.

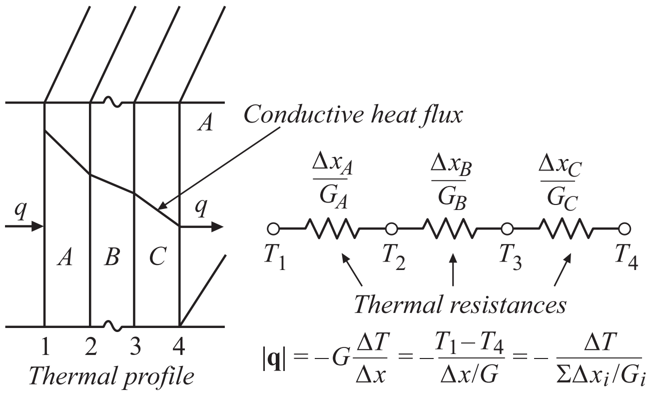

Figure 9. Thermal resistance model used to calculate the heat flux.

Table 5. Parameters of materials used to calculate the induced polarization of pyroelectric films on a silicon membrane

Material	C_p, $\frac{\text{J}}{\text{kg}\cdot\text{K}}$	G_{th}, $\frac{\text{W}}{\text{m}\cdot\text{K}}$	ρ, $\frac{\text{kg}}{\text{m}^3}$	γ	p, $\frac{\mu\text{C}}{\text{m}^2\cdot\text{K}}$
SBN50 (Barium strontium niobate)	440 [30]	1.8 [31]	5300 [31]	0.88 [32]	−400 [36]
PZT-5H (Lead zirconate titanate)	350 [33]	0.14	7500	1 [34]	−450 [36]
TGS *l*-alanine (Triglycine sulfate)	1352 [31]	1 [31]	1700	1 [35]	−550 [36]
Si	700	130	2329	0.2	–
SiO_2	703	0	2203	0.2	–

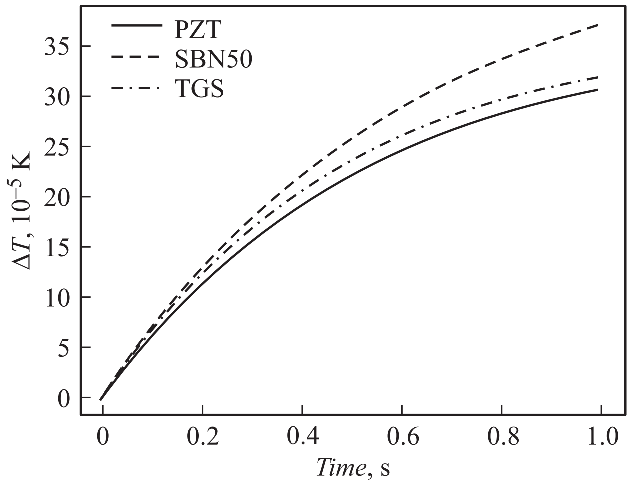

Figure 10. Temporal characteristic of temperature changes in different pyroelectric films induced by the incident heat flow.

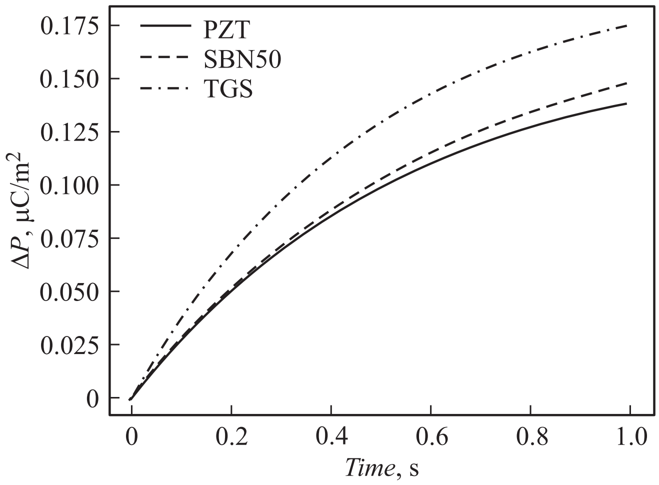

Figure 11. Temporal characteristic of polarization changes in different pyroelectric films induced by the incident heat flow.

$\sim 1\,\mu$W), and the duration of heat flow was assumed to be approximately equal to one second.

The results of film temperature changes dynamics calculation, which was performed in accordance with the mentioned model (Fig. 9) with the use of Eqs. (15)−(17), are presented below (Fig. 10).

Equation (18) and the obtained data on temporal variations of temperature of the pyroelectric material (Fig. 10) were used to calculate the film polarization (Fig. 11) induced by the thermal field:

$$\Delta P_S = p\Delta T = p\big(T_{\text{initial}} - T(t)\big), \tag{18}$$

where T_{initial} is the initial temperature, p is the pyroelectric coefficient (Table 5), and ΔP_S is the polarization vector variation.

4. Dynamics of variation of the electric potentials in the pyroelectric films induced by the thermal field

Using Eq. (19) and the temporal characteristics of polarization variations $\Delta P_S(t)$ (Fig. 11), one may obtain a coordinate dependence of the electric potential on polarization induced by the thermal field at a fixed heat flow rate (see Appendix 2) and then calculate the electric potential at arbitrary distance z from the film surface at any point in time:

$$\Delta\phi(z) = \frac{\Delta P_S}{2\varepsilon_0}\Big(\sqrt{(z+d)^2 + R^2} - \sqrt{z^2 + R^2} - d\Big). \tag{19}$$

Specifically, the temporal characteristics of changes in surface electric potential $\Delta\phi(t)$ for different pyroelectric films at $z \approx 0$ and a heat flow density of $0.21\,\mu\text{W/cm}^2$ are presented below (Fig. 12).

5. Estimation of the probable influence of elastic deformation on the electric potentials in the pyroelectric film induced by the thermal field

In the proposed design of a thermal image receiver the pyroelectric film is mounted on the oxidized surface of a thin silicon membrane (to minimize the heat loss due to thermal conductivity). Owing to the significant difference in thermal expansion coefficients of individual

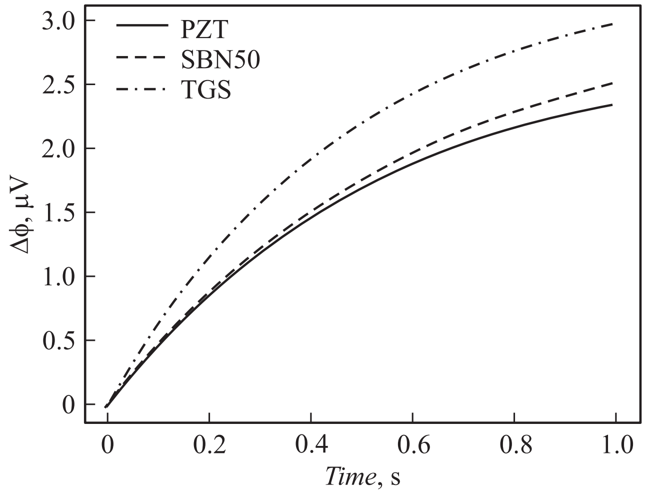

Figure 12. Temporal characteristic of changes in the surface potential ($z \approx 0$) for different pyroelectric films induced by a spontaneous polarization change.

Table 6. Thermal expansion coefficients of the materials used in this study

Material	α, $\frac{10^{-6}}{\mathrm{K}}$
Si	2.6
SiO_2	0.55
PZT-5H	3.6

heterostructure layers, the distribution pattern of electric potentials induced by the thermal field may be distorted due to the piezoelectric effect. The contribution of the oxide coating to the resulting elastic stress is neglected in our calculations (see Table 2 for justification). Distortions of the distribution pattern of electric potentials on the pyroelectric film surface associated with temperature variations due to the piezoelectric effect were simulated for specific materials (Table 6). The rationale behind these calculations and the calculation procedure are presented in Appendix 5.

The calculations performed in COMSOL Multiphysics made it possible to obtain plots of averaged values of the electric polarization, the electric potential, and the electric-field intensity on the pyroelectric surface caused only by deformations. The calculation results are presented in Figs. 13–15.

Inserting the maximum value of polarization of the pyroelectric material (it was $P_{piezo} = 50\,\frac{nC}{m^2}$) into Eq. (19), we obtain an estimate of the surface potential induced by the piezoelectric effect. This estimate is $\sim \Delta\phi = 0.8\,\mu\mathrm{V}$ at dipole displacement vector length $d = 0.3\,\mathrm{nm}$ of the dipole layer.

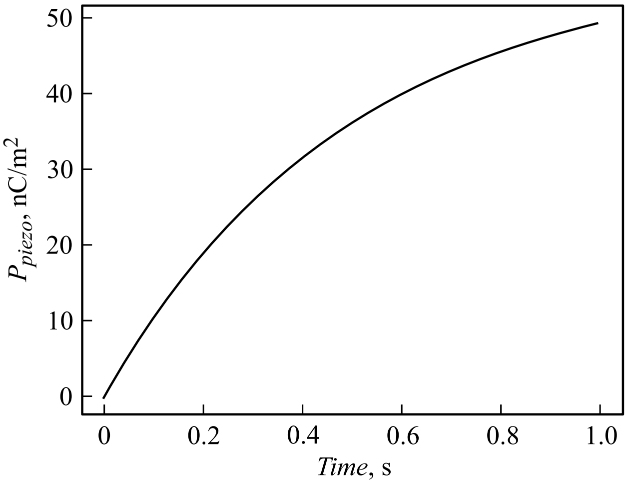

Figure 13. Temporal characteristic of piezoelectric polarization ($z \approx 0$), which is associated with deformation of the multilayer structure due to thermal expansion, of the pyroelectric sample.

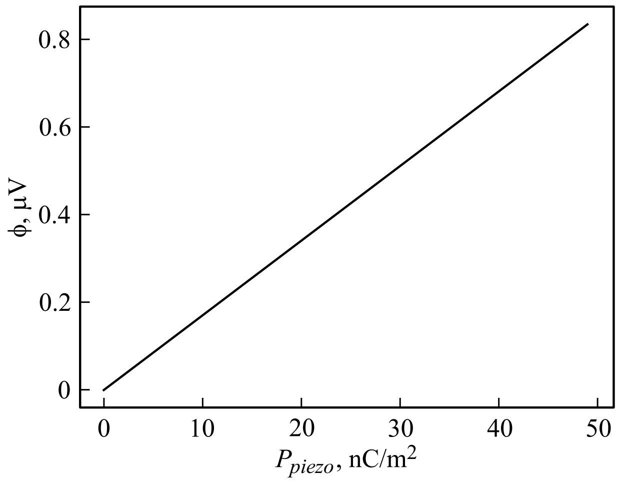

Figure 14. Dependence of the surface potential of the pyroelectric sample on the piezoelectric polarization value.

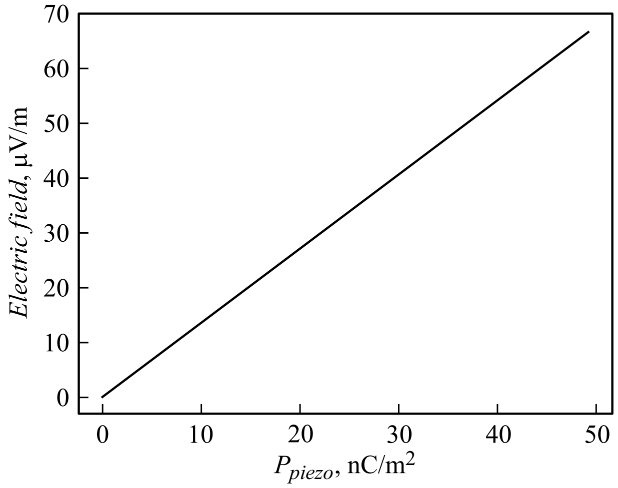

Figure 15. Dependence of the electric-field intensity of the pyroelectric sample on the piezoelectric polarization value.

6. Calculated characteristics of pyroelectric films integrated into the structure of an innovative thermal image receiver

The estimated performance limits of thermal image receivers with specific types of sensing pyroelectric films are listed in Table 7. The calculation procedure is presented in Appendix 6.

Table 7. Results of calculation of polarization and the surface potential for different pyroelectric samples

Material	D, cm$\sqrt{Hz}$/W $S = 16 \times 16\,\mu$m	$\mathscr{R}$, $\frac{\text{V}}{\text{W}}$	NEP, nW/$\sqrt{Hz}$	V_N, nV
SBN50	10^6	3.7	17.8	178
PZT-5H	$8.7 \cdot 10^5$	3.1	17.8	178
TGS with the addition l-alanine	$2.84 \cdot 10^5$	3.2	56.3	563

Note. The notation is the same as in Table 1.

Conclusion

An innovative single-channel design of a thermal image receiver ($3-15\,\mu$m) in the IIT architecture was examined. The processes of spontaneous polarization of a pyroelectric sensing and conversion film and its polarization induced by a thermal field were discussed. A pyroelectric film serves as a thermal sensor and converter. The spatial distribution of the electric potential induced by a thermal image near the surface of the pyroelectric film is read out by a photoelectrons flux in the „shot-through“ mode via apertures in a Si/SiO$_2$ membrane. This photoelectrons flux is produced by a photocathode, which positioned at the end face of the entrance window, and carries information regarding the surrounding terrain in reflected night sky light in the near-infrared range ($0.8-1.1\,\mu$m). The results of functional dependences calculations of the electric-field intensity and electric potentials on the characteristics of spontaneous film polarization were presented graphically and in tabular form.

For a number of pyroelectric films, estimates have been obtained for the conversion efficiency of the thermal fields projected onto the film into the distribution pattern of electric potentials. The probable parasitic contributions of piezoelectric effects in the bimorph (pyroelectric film/silicon membrane) structure to the distribution pattern of electric potentials was taken into account. The key performance limits of the sensing and conversion unit of the considered thermal image receiver were estimated.

Appendix 1

The field intensity of the upper plane is

$$E_{\text{upper plane}} = -\frac{P_S z}{4\pi\varepsilon_0} \int\limits_0^R \int\limits_0^{2\pi} \frac{r}{(z^2+r^2)^{3/2}}\, dr d\varphi \tag{A1.1}$$

Therefore,

$$E_{\text{upper plane}} = -\frac{P_S z}{2\varepsilon_0} \int\limits_0^R \frac{r}{(z^2+r^2)^{3/2}}\, dr \tag{A1.2}$$

and, performing a substitution of variables, we obtain

$$E_{\text{upper plane}} = -\frac{P_S z}{4\varepsilon_0} \int\limits_0^R \frac{d(r^2+z^2)}{(z^2+r^2)^{3/2}}. \tag{A1.3}$$

Thus, we derive the functional dependence of electric-field intensity E of the upper negatively charged plane of the dipole layer from expression (5):

$$E_{\text{upper plane}} = \left(\frac{P_S}{2\varepsilon_0} \frac{z}{\sqrt{z^2+r^2}}\right)\Bigg|_0^R = -\frac{P_S}{2\varepsilon_0}\left(1 - \frac{z}{\sqrt{z^2+R^2}}\right). \tag{A1.4}$$

Appendix 2

The integral of a superposition of electric-field intensities of both planes is

$$\varphi(z) = -\int\limits_\infty^z \frac{P_S}{2\varepsilon_0}\left(\frac{z}{\sqrt{z^2+R^2}} + \frac{z+d}{\sqrt{(z+d)^2+R^2}}\right) dz. \tag{A2.1}$$

Its antiderivative is

$$\varphi(z) = \frac{P_S}{2\varepsilon_0}\left(\sqrt{(z+d)^2+R^2} - \sqrt{z^2+R^2}\right)\Bigg|_\infty^z. \tag{A2.2}$$

Let us consider the lower limit of function (A2.2):

$$\lim_{z\to\infty} \frac{P_S}{2\varepsilon_0}\left(\sqrt{(z+d)^2+R^2} - \sqrt{z^2+R^2}\right). \tag{A2.3}$$

Transforming (A2.3) and expanding the obtained expression into a Taylor series (utilizing the smallness of $\frac{2zd+d^2}{z^2+R^2}$ at $z \to \infty$), we find

$$\lim_{z\to\infty} \frac{P_S}{2\varepsilon_0} \sqrt{z^2+R^2}\left(1 + \frac{2zd+d^2}{2(z^2+R^2)} - 1\right) = \frac{P_S}{2\varepsilon_0} d. \tag{A2.4}$$

Inserting (A2.4) into expression (A2.2), we obtain a functional dependence for the electric potential of arbitrary point z:

$$\varphi(z) = \frac{P_S}{2\varepsilon_0}\left(\sqrt{(z+d)^2+R^2} - \sqrt{z^2+R^2} - d\right). \tag{A2.5}$$

Appendix 3

Let us present expression (5) from the main text in the form

$$E = \frac{P_S}{2\varepsilon_0}\frac{2}{\sqrt{z^2+R^2}}\left(z - \frac{z+d}{\sqrt{1+\frac{2zd+d^2}{z^2+R^2}}}\right). \tag{A3.1}$$

Expanding (A3.1) into a Taylor series, we obtain the following after several transformations at $R \gg z$:

$$E = \frac{P_S}{2\varepsilon_0}\frac{1}{R}\left(z - \frac{2(z+d)R^2}{2R^2+2zd+d^2}\right) = -\frac{P_S}{2\varepsilon_0} \times \frac{2(z+d)R}{2R^2+2zd+d^2} = -\frac{P_S}{2\varepsilon_0}\frac{(z+d)}{R}. \tag{A3.2}$$

If dipole arm $d \gg z$, it follows from expression (A3.2) that

$$E = -\frac{P_S}{2\varepsilon_0}\frac{d}{R}. \tag{A3.3}$$

Proceeding in a similar way, we derive an approximation for the electric potential from Eq. (A2.5) at $R \gg z$:

$$\varphi(z) = \frac{P_S}{2\varepsilon_0}\sqrt{z^2+R^2}\left(\sqrt{1+\frac{2zd+d^2}{z^2+R^2}} - 1 - \frac{d}{\sqrt{z^2+R^2}}\right). \tag{A3.4}$$

Using the Taylor series expansion, we find from (A3.4) that

$$\varphi(z) = \frac{P_S}{2\varepsilon_0}\sqrt{z^2+R^2}\left(1+\frac{2z_0d+d^2}{2(z^2+R^2)} - 1 - \frac{d}{\sqrt{z^2+R^2}}\right). \tag{A3.5}$$

Since $R \gg z$, expression (A3.5) may be transformed into

$$\varphi(z) = \frac{P_S}{2\varepsilon_0}R\left(\frac{2zd+d^2}{2R^2} - \frac{d}{R}\right). \tag{A3.6}$$

In the $2zd \gg d^2$ case, expression (A3.6) is transformed into (A3.7):

$$\varphi(z_0) = \frac{P_S}{2\varepsilon_0}\left(\frac{zd}{R} - d\right). \tag{A3.7}$$

Appendix 4

In order to determine the functional dependence for the electric potential at $z \gg R$, we integrate expression (13) from the main text:

$$\Delta\varphi_{\text{upper plane}} = -\int_{\infty}^{z} -\frac{P_SR^2}{2\varepsilon_0}\frac{d}{z^3}\,dz = -\left.\frac{P_SR^2d}{4\varepsilon_0 z^2}\right|_{\infty}^{z}. \tag{A4.1}$$

Thus, the potential of the dipole layer at arbitrary point z at $z \gg R$ is

$$\varphi(z) = -\frac{P_SR^2}{4\varepsilon_0}\frac{d}{z^2}. \tag{A4.2}$$

Appendix 5

Let us use the expression for the mechanical stress tensor to estimate the probable distortion of the distribution of electric potentials induced by the piezoeffect:

$$S_{ij} = \sum_{kl} C_{ijkl}\varepsilon_{kl} - \sum_{mn} e_{ijmn}E_{mn}. \tag{A5.1}$$

Here, S_{ij} is the mechanical stress tensor, C_{ijkl} is the tensor of elastic constants, ε_{kl} is the deformation tensor ($\varepsilon_{kl} = \alpha_{kl}\Delta T$), e_{ijmn} is the tensor of piezoelectric coefficients, and E_{mn} is the electric-field intensity tensor; α_j is the matrix of thermal expansion coefficients and ΔT is the change in temperature of the studied material.

We use the Cauchy–Green form of the deformation tensor:

$$\varepsilon_{kl} = \frac{1}{2}\left(\frac{\partial u_k}{\partial x_l} + \frac{\partial u_l}{\partial x_k}\right), \tag{A5.2}$$

where $\mathbf{u}$ is the vector characterizing displacements.

A simultaneous solution of Eqs. (A5.1), (A5.2) with the use of the finite element method allows one to calculate deformations ε_{kl} as functions of temperature $T(t)$. The obtained deformation values at different temperatures $\varepsilon_{kl}(T(t))$ are used to calculate the electric flux density:

$$D_{ij} = \sum_{kl} e_{ijkl}\varepsilon_{kl} + \sum_{mn} \varepsilon_{ijmn}E_{mn}, \tag{A5.3}$$

where ε_{ijmn} is the permittivity tensor of the piezoelectric material. Assuming that the external field is zero ($\mathbf{E}_{\text{external}} = 0$), the following relation is obtained for electric flux density (A5.3):

$$\mathbf{D} = \mathbf{P}_{piezo}. \tag{A5.4}$$

Inserting the values of piezoelectric polarization $\mathbf{P}_{piezo}$ into Eq. (19) from the main text, which characterizes the overall pattern of the potential distribution regardless of the cause of polarization, we determine the surface potential induced by elastic deformations.

In doing this, we use

tensor of piezoelectric coefficients e_{ijkl} for PZT

$$e_{ijkl} = \begin{pmatrix} 0 & 0 & 0 & 17.034 & 0 & 0 \\ 0 & 0 & 0 & 0 & 0 & 0 \\ -6.62281 & -6.62281 & 23.24 & 0 & 0 & 0 \end{pmatrix}\left[\frac{\mathrm{C}}{\mathrm{m}^2}\right], \tag{A5.5}$$

tensor of elastic constants C_{ijkl} for PZT

$$C_{ijkl} = \begin{pmatrix} 127.2 & 80.21 & 84.67 & 0 & 0 & 0 \\ 80.21 & 127.2 & 84.67 & 0 & 0 & 0 \\ 84.67 & 84.67 & 117.43 & 0 & 0 & 0 \\ 0 & 0 & 0 & 22.98 & 0 & 0 \\ 0 & 0 & 0 & 0 & 22.98 & 0 \\ 0 & 0 & 0 & 0 & 0 & 23.47 \end{pmatrix}[\mathrm{GPa}] \tag{A5.6}$$

and tensor of elastic constants C_{ijkl} for Si

$$C_{ijkl} = \begin{pmatrix} 166 & 64 & 64 & 0 & 0 & 0 \\ 64 & 166 & 64 & 0 & 0 & 0 \\ 64 & 64 & 166 & 0 & 0 & 0 \\ 0 & 0 & 0 & 80 & 0 & 0 \\ 0 & 0 & 0 & 0 & 80 & 0 \\ 0 & 0 & 0 & 0 & 0 & 80 \end{pmatrix} \text{[GPa]}. \quad \text{(A5.7)}$$

Appendix 6

Let us use literature data on resistivities of the examined films (Table A6.1).

Table A6.1. Resistivities of pyroelectric films used in calculations for the double-layer Si membrane/pyroelectric structure

Pyroelectric material	Resistivity ρ_R, $\Omega \cdot$ m
SBN50	10^7 [37]
PZT-5H	10^7
TGS *l*-alanine	10^8 [38]

Since Johnson noise is the dominant type of noise in thermal imaging [39], we use the following expression to estimate the thermal noise level:

$$V_N = \sqrt{4kTR\Delta f}, \qquad \text{(A6.1)}$$

where k is the Boltzmann constant, T is the temperature of the sensing and conversion sample, R is the resistance of the sensing and conversion sample, and Δf is the equivalent frequency passband.

Having calculated the thermal noise level, we obtain the following for the ultimate sensitivity of pyroelectric image receivers:

$$\mathscr{R} = \frac{\Delta\phi}{P}. \qquad \text{(A6.2)}$$

The results of calculation of the key parameters of sensing and conversion materials, which were determined in this study for specific types of pyroelectric films, are presented in Table 4 in the main text.

Funding

This research was supported financially by the Russian Foundation for Basic Research as part of research project No. 20-38-90125.

Conflict of interest

The authors declare that they have no conflict of interest.

References

[1] C. Jelen, S.B. Slivken, T. David, G. Brown, M. Razeghi. In: *Photodetectors: Materials and Devices III,* ed. by G.J. Brown (San Jose, Proc. SPIE, 1998), v. 3287, p. 96–104. DOI: 10.1117/12.304470

[2] O.O. Cellek, S. Ozer, C. Besikci. IEEE J. Quant. Electron., **41** (7), 980 (2005). DOI: 10.1109/JQE.2005.848947

[3] S.U. Eker, Y. Arslan, C. Besikci. Infrared Phys. Technol., **54** (2), 209 (2011). DOI: 10.1016/j.infrared.2010.12.015

[4] L.T. Chee, M. Hooman. Nanophotonics, **7** (1), 1 (2017). DOI: 10.1515/nanoph-2017-0061

[5] V.V. Korotaev, G.S. Mel'nikov, S.V. Mikheev, V.M. Samkov, Yu.I. Soldatov. *Osnovy teplovideniya* (St. Petersburg: NIU ITMO, St. Petersburg, 2012), p. 122 (in Russian).

[6] J.E. Huffman, A.G. Crouse, B.L. Halleck, T.V. Downes. J. Appl. Phys., **72** (1), 273 (1998). DOI: 10.1063/1.352127

[7] N. Sclar. In: *Infrared Detectors,* ed. by W.L. Wolfe (San-Diego, Proc. SPIE, 1983), v. 0443, p. 11–41. DOI: 10.1117/12.937937

[8] S.M. Birkmann, J. Stegmaier, U. Grözinger, O. Krause. In: *High Energy, Optical, and Infrared Detectors for Astronomy III,* ed. by D.A. Dorn, A.D. Holland (Marceille, Proc, SPIE, 2008), v. 7021, p. 70210R. DOI: 10.1117/12.789103

[9] S.I. Woods, J.E. Proctor, T.M. Jung, A.C. Carter, J. Neira, D.R. Defibaugh. Appl. Opt., **57** (18), D82 (2018). DOI: 10.1364/AO.57.000D82

[10] A. Rogalski. Infrared Phys. Technol., **43** (3–5), 187 (2002). DOI: 10.1016/S1350-4495(02)00140-8

[11] G. Eppeldauer, M. Rácz. Appl. Opt., **39** (31), 5739 (2000). DOI: 10.1364/AO.39.005739

[12] H. Yuan, G. Apgar, J. Kim, J. Laquindanum, V. Nalavade. *Infrared Technology and Applications XXXIV,* ed. by B.F. Andersen, G.F. Fulop, P.R. Norton (Orlando, Proc. SPIE, 2008), v. 6940, p. 69403C. DOI: 10.1117/12.782735

[13] A. Rogalski. Infrared Phys. Technol., **54** (5), 126 (2011). DOI: 10.1016/j.infrared.2010.12.003

[14] I.E. Carranza, J. Grant, J. Gough, R.S. David. IEEE Trans. Terahertz Sci. Technol., **5** (6), 892 (2015). DOI: 10.1109/TTHZ.2015.2463673

[15] Y.-Z. Deng, S.-F. Tang, H.-Y. Zeng, Z.-Y. Wu, D.-K. Tung. Sensors (Basel), **18** (2593), 1 (2018). DOI: 10.3390/s18082593

[16] M.F. Rashman, I.A. Steele, S.D. Bates, D. Copley, S.N. Longmore. Monthly Notices Royal Astronom. Society, **492** (1), 480 (2020). DOI: 10.1093/mnras/stz3497

[17] C. Vedel, J.-L. Martin, J.-L. Ouvrier Buffet. In: *Infrared Technology and Applications XXV,* ed. by B.F. Andersen, M. Strojnik (Orlando, Proc. SPIE, 1999), v. 3698, p. 276–283. DOI: 10.1117/12.354529

[18] T. Schimert, D. Ratcliff, J. Brady, S. Ropson, R. Gooch, B. Ritchey, P. McCardel, K. Rachels, M. Wand, M. Weinstein, J. Wyim. In: *Unattended Ground Sensor Technologies and Applications,* ed. by E.M. Carapezza, D.B. Law, K.T. Stalker (Orlando, Proc. SPIE, 1999), v. 3713, p. 101–111. DOI: 10.1117/12.357125

[19] S. Estill, M.R. Brozel. MRS Online Proceed. Library, **299**, 27 (1994). DOI: 10.1557/PROC-299-27

[20] C. Hoffman, R. Driggers. *Encyclopedia of Optical and Photonic Engineering (Print) — Five Volume Set* (CRC Press, Florida, 2015), p. 4088. ISBN: 9781439850978

[21] F.J. Low. J. Optical Society America, **51** (11), 1300 (1961). DOI: 10.1364/JOSA.51.001300

[22] M.A. Tarasov, L.S. Kuzmin, V.S. Edelman, N.S. Kaurova, M.Yu. Fominskii, A.B. Ermakov. JETP Lett., **92**, 416 (2010). DOI: 10.1134/S0021364010180116

[23] A. Rogalski. *Infrared Detectors: 2nd ed.* (CRC Press, Florida, 2020), p. 898. ISBN: 9780367577094

[24] S.K. Holland, R.H. Krauss, G. Laufer. Optical Engineer., **43** (10), 2303 (2004). DOI: 10.1117/1.1782612

[25] C.B. Roundy, R.L. Byer. J. Appl. Phys., **44** (2), 929 (1973). DOI: 10.1063/1.1662294

[26] M.C. Kao, H.Z. Chen, S.L. Yang, Y.C. Chen, P.T. Hsieh, C.C. Yu. Thin. Solid Films, **516** (16), 5518 (2008). DOI: 10.1016/j.tsf.2007.07.020

[27] C. Giebeler, J. Wright, S. Freeborn, N. Conway, T. Chamberlain, P. Clark, M. Schreiter, D. Pitzer, R. Koehle. *SENSOR + TEST Conference 2009* (Nürnberg, AMA Service GmbH, 2009), p. 185–189. DOI: 10.5162/irs09/i1.1

[28] C.M. Dudhe, S.B. Nagdeote, C. P. Chaudhari. Taylor & Francis, Ferroelectrics, **482**, 104 (2015). DOI: 10.1080/00150193.2015.1057080

[29] W.R. Cook, jr. *Piezoelectric, Pyroelectric, and Related Constants* (Springer-Verlag, Berlin, Heidelberg, Berlin, 1994), p. 543. ISBN: 978-3-540-55065-5

[30] S.T. Liu, R.B. Maciolek. J. Electron. Mater., **4** (1), 91 (1975). DOI: 10.1007/BF02657838

[31] H.V. Alexandru, C. Berbecaru, F. Stanculescu, L. Pintilie, I. Matei, M. Lisca. Sensors Actuators A: Phys., **113** (3), 387 (2004). DOI: 10.1016/j.sna.2004.03.046

[32] W.A. Tiller. *The Science of Crystallization Macroscopic Phenomena and Defect Generation* (Cambridge University Press, California, 1992), p. 520. ISBN: 9780521388283

[33] S. Yarlagadda, H.W. Chan, H. Lee. J. Intelligent Mater. Systems Structures, **6** (6), 757 (1995). DOI: 10.1177/1045389X9500600603

[34] J. Ouyang. *Enhanced Piezoelectric Performance of Printed PZT Films on Low Temperature Substrates* (Rochester, Rochester Institute of Technology, 2017)

[35] T.A. Germer, J.C. Zwinkels, B.K. Tsai. *Spectrophotometry: Accurate Measurement of Optical Properties of Materials* (Amsterdam, Academic Press, 2014), v. 46, p. 533. ISBN: 9780123860224

[36] W.R. Cook, jr. *Piezoelectric, Pyroelectric, and Related Constants* (Springer-Verlag, Berlin, Heidelberg, Berlin, 1994), p. 543. ISBN: 978-3-540-55065-5

[37] L. Zhang, R. Barrett, P. Cloetens, C. Detlefs, M. Sanchez del Rio. J. Synchrotron Rad., **21**, 507 (2014). DOI: 10.1107/S1600577514004962

[38] Y. Wu, G. Caoa. J. Mater. Res., **15** (7), 1583 (2000). DOI: 10.1557/JMR.2000.0227

[39] M. Vollmer, K.-P. Mollmann. *Infrared Thermal Imaging Fundamentals, Research and Applications* (Wiley-VCH, 2018), p. 794. ISBN: 978-3-527-41351-5